Evaluation of the Oxygen Mobility in CePO 4 -Supported Catalysts: Mechanistic Implications on the Water–Gas Shift Reaction

Sara Navarro-Jaén, Luis Bobadilla, Francisca Romero-Sarria, Oscar Laguna, Nicolas Bion, José Odriozola

Evaluation of the Oxygen Mobility in $CePO_4$-Supported Catalysts: Mechanistic Implications on the WGS Reaction

Sara Navarro-Jaén*,▽,†, Luis F. Bobadilla▽, Francisca Romero-Sarria▽, Oscar H. Laguna▽,#, Nicolas Bion‡, José A. Odriozola▽

▽Departamento de Química Inorgánica e Instituto de Ciencia de Materiales de Sevilla, Centro Mixto Universidad de Sevilla- CSIC, Av. Américo Vespucio 49, 41092 Seville, Spain

‡ Institut de Chimie des Milieux et Matériaux de Poitiers (IC2MP), Université de Poitiers- CNRS, 4 rue Michel Brunet, TSA51106, F86073 Poitiers Cedex 9, France

*Corresponding author: snavarro3@us.es

ABSTRACT: The hexagonal and monoclinic phases of $CePO_4$ have demonstrated to be excellent catalytic supports for Pt-based WGS catalysts. Consequently, the elucidation of the WGS reaction mechanism in these materials constitutes a fundamental aspect in order to explain their catalytic behavior. Since the observed WGS reaction path is closely related to the absence or presence of oxygen vacancies in the support, the study of the oxygen mobility in these solids constitutes a key factor for the understanding of the materials structure and its influence on the reaction mechanism. In this study, the oxygen mobility in the $CePO_4$ supports and the corresponding Pt catalysts has been evaluated by means of isotopic exchange experiments using $^{18}O_2$ and $C^{18}O_2$ as probe molecules. Results demonstrate that the evaluated solids present a low exchange activity when $^{18}O_2$ is used, indicating the absence of oxygen vacancies in these solids and thus, suggesting a poor influence of the WGS redox mechanism. On the contrary, a high oxygen exchange activity is observed using $C^{18}O_2$, demonstrating that the exchange in these materials takes place through the formation of carbonate-like intermediates, and thus suggesting the associative mechanism of the WGS reaction as the preferred path in these solids. *Operando* DRIFTS experiments under WGS reaction conditions confirm these results, proving that the WGS reaction in the studied materials takes place through a formate-mediated associative mechanism.

1. INTRODUCTION

The use of hydrogen as energy carrier combined with the development of fuel cells have gained increasing interest in the last years. Particularly, polymer electrolyte membrane fuel cells (PEMFCs) constitute the most promising option for portable applications. However, the purification of the hydrogen used as feed in these systems results mandatory [1]. Among the fuel processing reactions used with this objective, the water-gas shift (WGS) reaction is the most relevant step, since it removes the highest CO content while increasing the H_2 content [2].

In this context, oxide-supported noble metal catalysts have been extensively studied and have demonstrated to be excellent WGS catalysts for fuel cell applications [3-4]. However, in the last few years some studies have been devoted to the use of phosphate-type solids as WGS catalytic supports [5-7].

In a previous work [8], we reported the use of $Pt/CePO_4$ catalysts as highly active and selective catalytic systems for the WGS reaction. $CePO_4$ can present two different crystal structures: the hexagonal (rhabdophane-type) phase, which contains structural channels able to hold water molecules and the monoclinic (monazite-type) phase, in which the vanishing of the structural channels takes place. We studied the influence of the support structure on the WGS catalytic activity, concluding that the rhabdophane-type phase (CeP400) enhanced the WGS catalytic performance with respect to the monazite-type phase (CeP600) as a consequence of an enhanced water adsorption capacity of the support, which allowed a continuous water supplying during the reaction.

Since phosphate-type solids constitute a promising option as WGS catalytic supports [5-7], the understanding of the WGS reaction mechanism in these solids results of great interest.

Although WGS reaction mechanism has been thoroughly studied [4, 9-12], the reaction path is still a matter of debate. However, two mechanisms have been generally proposed: the *redox* and the *associative* mechanism, which imply both the participation of the metal phase and the support [13-15].

In the *redox* mechanism, the oxidation-reduction cycles occurring in the support are responsible for the WGS reaction. CO adsorbs on metal sites and reacts with the oxygen of the support to yield CO_2, thus generating an oxygen vacancy. Afterwards, the generated oxygen vacancy is re-oxidized by H_2O. The interaction of water with the vacancies of the solid generates OH and eventually, H groups. This mechanism has been typically observed on partially reduced oxides containing oxygen vacancies, such as TiO_2, CeO_2 or CeO_2/ZrO_2 [13].

On the contrary, the *associative* mechanism is an adsorption-desorption model where the adsorbed species interact to form an adsorbed intermediate which decomposes into the reaction products. Thus, it implies the adsorption of CO and H_2O on the catalyst surface to form surface intermediates such as formate, carbonate or carbonyl species, that decompose into the reaction products, CO_2 and H_2 [4, 13, 16].

According to the aforementioned aspects, the structure and more specifically, the presence or not of oxygen vacancies has demonstrated to play a substantial role regarding the WGS reaction mechanism in oxide-supported catalysts [9, 17-18]. Consequently, studying the mobility of the oxygen atoms contained in the solids become of great interest in order to justify the reaction path followed by the catalysts under study. In this context, isotopic exchange techniques using molecules containing ^{18}O provide answers to characterize the catalysts behavior regarding the mobility and reactivity of the oxygen atoms constituting the solid, as well as the elucidation of reaction mechanisms [19-20]. Generally, the exchange reaction mechanism includes three main steps [21]:

1. Adsorption and subsequent dissociation of the labelled molecule ($^*X_2$) to form atoms or ions adsorbed on the surface ($^*X_{ads}$).

2. Exchange of such species ($^*X_{ads}$) with the atoms or ions naturally present in the surface or the bulk of the solid (X_s).

3. Desorption of the exchanged elements in their molecular form ($^*X_2$, X_2 or $^*XX$) in the gas phase.

Additionally, diffusion phenomena can take place if the adsorbed labelled species and those present in the solid are not in the same region of the catalyst after the adsorption of the labelled molecule.

The change in the gas phase composition during the exchange reaction allows to calculate characteristic parameters of the isotopic exchange as the atomic fraction of ^{18}O in the gas phase, the rate of exchange, the diffusion coefficients on the surface and in the bulk and the number of exchanged and exchangeable oxygen atoms in the catalyst, which are useful parameters for the knowledge of the catalytic properties of the solids [21].

Particularly, isotopic exchange using $^{18}O_2/^{16}O_2$ and $C^{18}O_2/C^{16}O_2$ is a powerful technique for the study of the WGS reaction mechanism. Differences in the oxygen rate of exchange depending on the labelled molecule are a consequence of a difference in the exchange mechanism: in the case of oxygen, a dissociative mechanism in which the rate limiting step is the dissociation of the oxygen molecule, whereas in the case of CO_2 an associative mechanism takes place, *via* formation and decomposition of intermediate species such as carbonate, hydrogen carbonate or formate species [22].

Consequently, the isotopic exchange experiments using $^{18}O_2$ result of great interest for evaluating the absence or presence of oxygen vacancies in the supports, which play an important role in the WGS *redox* mechanism. On the other hand, experiments using $C^{18}O_2$ allow the evaluation of the formation of carbonate-like intermediate species, implied in the WGS *associative* mechanism. Thus, the use of these labelled molecules could provide information about the preferred mechanism and/or the competence between them, which are crucial aspects during the WGS reaction.

According to the aforementioned considerations, this work presents the study of the oxygen mobility in two types of $CePO_4$ supports with different structure and the corresponding WGS Pt catalysts by means of isotopic exchange techniques. *Operando* Diffuse Reflectance Infrared Spectroscopy (DRIFTS) was employed to obtain mechanistic insights, in order to correlate the inherent oxygen mobility of the solids to the observed WGS reaction mechanism.

2. EXPERIMENTAL SECTION

$CePO_4$ supports were prepared by a hydrothermal method previously described [8]. The obtained materials were calcined in air at two different temperatures: 400 °C, to obtain the rhabdophane-type phase of $CePO_4$ (CeP400), and 600 °C to obtain the monazite-type phase (CeP600). Pt catalysts with a nominal content of 2 wt.% were prepared by wet impregnation and calcined at 350 °C.

For the X^*/X (X= O_2, CO_2) isotopic exchange experiments of the evaluated samples, 20 mg of the solids were introduced in a quartz U reactor placed in a closed recirculation system, connected to a mass spectrometer in order to follow continuously the evolution of the gaseous species as a function of the time, and to a vacuum pump. A recirculation pump eliminated the limitations due to the gas phase diffusion. A scheme of the reaction system has been presented elsewhere [21].

The studied supports were first activated under 50 ml·min^{-1} of $^{16}O_2$ at the calcination temperature and atmospheric pressure. Regarding the catalysts, the activation was carried out at 350 °C under 50 ml·min^{-1} of H_2 in order to ensure the reduction of the metallic species. Subsequently, the temperature was decreased and the activation gas was evacuated to introduce the isotopic molecule in the reaction system. For the heteroexchange experiments, 65 mbar of $^{18}O_2$ (Sigma-Aldrich, 99.9%) or $C^{18}O_2$ (Sigma-Aldrich, 97%) were introduced in the system. Two different experiments were performed:

Temperature programmed isotopic exchange (TPIE), where the temperature was progressively increased along the experiment at a rate of 2 °C·min^{-1}.

Isothermal isotopic exchange (IIE), where the temperature was kept constant along the experiment.

During the $^{18}O_2/^{16}O_2$ isotopic exchange experiments, the mass-to-charge ratio (m/z) 32 ($^{16}O_2$), 34 ($^{16}O^{18}O$) and 36 ($^{18}O_2$) were recorded, whereas for the $C^{18}O_2/C^{16}O_2$ isotopic exchange experiments, the mass-to-charge ratio (m/z) 44 ($C^{16}O_2$), 46 ($C^{16}O^{18}O$) and 48 ($C^{18}O_2$) were evaluated, with the purpose of following the isotopomer distribution during the isotopic exchange reaction. The absence of air during the experiment was verified by mass spectrometry in both cases.

The ^{18}O atomic fractions in the gas phase ($\alpha_{g,t}$) were calculated according to Equation (1a) for $^{18}O_2/^{16}O_2$ or Equation (1b) for $C^{18}O_2/C^{16}O_2$ heteroexchange experiments.

$$\alpha_{g,t} = \frac{1/2\, P_{34,t} + P_{36,t}}{P_{32,t} + P_{34,t} + P_{36,t}} \qquad (\mathbf{1a})$$

$$\alpha_{g,t} = \frac{1/2\, P_{46,t} + P_{48,t}}{P_{44,t} + P_{46,t} + P_{48,t}} \qquad (\mathbf{1b})$$

Where $\mathbf{P_{x,t}}$ corresponds to the partial pressure of the gaseous species of mass/charge x at time t.

The rate of exchange (R_e), Equation (2), is generally calculated by the initial rate method, that is taking into account the rate at the beginning of the exchange reaction.

$$R_e = -N_g \frac{d\alpha_g}{dt} \qquad (\mathbf{2})$$

Where $\mathbf{N_g}$ is the number of oxygen atoms in the gas phase at the beginning of the reaction, which can be calculated according to Equation (3).

$$N_g = \frac{2N_A \cdot P_T}{R}\left(\frac{V_r}{T_r} + \frac{V_c}{T_c}\right) \qquad (\mathbf{3})$$

Where N_A is the Avogadro number, P_T corresponds to the total pressure, R is the ideal gas constant, V_r and V_c are the volumes and T_r and T_c are the temperatures of the heated and non-heated parts of the reaction system respectively.

Finally, the number of oxygen exchanged atoms (N_e) was calculated according to Equation (4).

$$N_e = N_g(1 - \alpha_g) \qquad (\mathbf{4})$$

If the diffusion rate in the support network becomes significant, the kinetics of exchange can be explained using the model developed by Kakioka et al. [21, 23-24], based in the following premises:

- Surface exchange is fast, thus the isotopic equilibrium between the gas phase and the surface atoms is rapidly reached
- Bulk diffusion takes place in spherical particles

In such case, the kinetics of diffusion in the solid follows Equation (5).

$$-Ln\frac{\alpha_g}{\alpha^*} = \frac{2}{\pi}\frac{\rho A}{N_g}\sqrt{D,t} \qquad (\mathbf{5})$$

Where α^* is the value of α_g once the surface exchange is completed and bulk diffusion starts. Consequently, the coefficient of bulk diffusion can be calculated from the slope "a" of $Ln\alpha_g$ vs. $t^{1/2}$ for $t > t_A$. This equation is valid if α^* and $\alpha_g >> \alpha_s^0$.

Operando diffuse reflectance infrared spectroscopy (DRIFTS) measurements were performed in a high-temperature reaction chamber supported on a DRIFTS optical system (Praying Mantis, Harricks) with ZnSe windows. Spectra were collected by a Thermo Nicolet iS50 FT-IR spectrometer equipped with a liquid-nitrogen cooled MCT detector at a resolution of 4 cm^{-1} and an average of 64 scans. 40 mg of the finely ground solids were loaded in the catalytic cell and the reaction flow containing 4.5% CO (Linde, ≥99.5%) and 10% H_2O in Ar (Air Liquide, ≥99.999%) with a total flow rate of 50 ml·min^{-1} was introduced using a series of AALBORG mass-flow controllers and a KNAUER Smartline 1050 HPLC pump for the introduction of water in the system. The system was heated at 100 °C to avoid water condensation during the reaction. Experiments were performed every 50 °C from 150 to 350 °C, previous activation of the samples at 350 °C under 50 ml·min^{-1} of 10% H_2 (Linde, ≥99.999%)/Ar (Air Liquide, ≥99.999%) flow.

CO_2 concentration at the exit of the reaction chamber was measured using a VAISALA GMT220 series detector.

Acquisition and analysis of DRIFTS spectra were carried out using OMNIC 8 (Thermo Scientific ®) software. For IR band heights normalization, band intensities were re-scaled to the unit interval, using a second order polynomial for baseline correction.

3. RESULTS AND DISCUSSION

3.1. $^{18}O_2/^{16}O_2$ isotopic exchange experiments

3.1.1. Isothermal $^{18}O_2/^{16}O_2$ isotopic exchange

In order to study the presence of oxygen vacancies, the oxygen mobility in the $CePO_4$-based solids was firstly evaluated using $^{18}O_2$ in isothermal conditions. The selected temperature to carry out these experiments was 300 °C, considering the high WGS activity of the $CePO_4$-based catalysts at this temperature [8] (See Supporting Information, **Figure S1**).

The evolution of the O_2 isotopic distribution as a function of the time during the exchange experiment at 300 °C on the CeP400 support is presented in Figure 1. At this temperature, the concentration of $^{18}O_2$ does not decrease, whereas no formation of $^{16}O^{18}O$ and/or $^{16}O_2$ is detected, indicating that the oxygen exchange is not significant in this support. Similar results were obtained for the CeP600 support and the corresponding Pt catalysts (not presented).

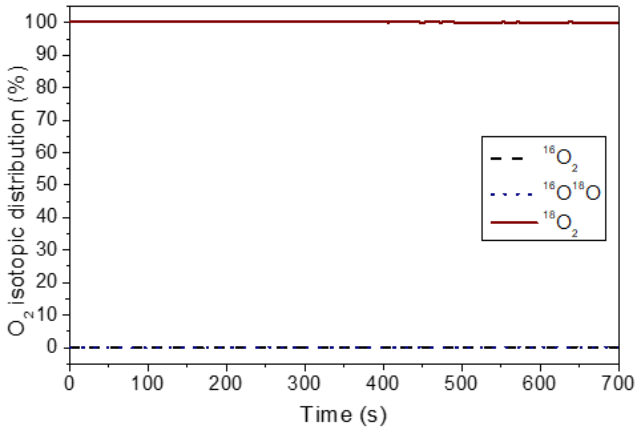

Figure 1. O_2 isotopic distribution (%) as a function of the time during isotopic exchange reaction at 300 °C over CeP400

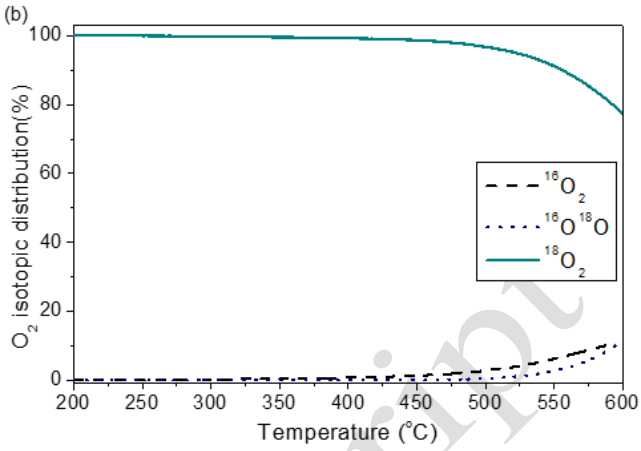

Figure 2. O_2 isotopic distribution (%) as a function of the temperature during temperature-programmed isotopic exchange reaction over (a) CeP400, (b) CeP600

3.1.2. Temperature- programmed $^{18}O_2/^{16}O_2$ isotopic exchange experiments

Since every solid presented no activity towards oxygen exchange at 300 °C, temperature programmed exchange experiments were carried out to evaluate the oxygen exchange capacity as a function of the temperature.

Results corresponding to the $CePO_4$ supports are displayed in Figure 2.

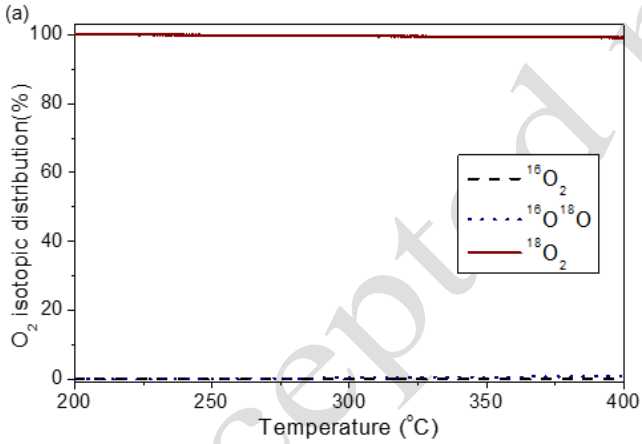

In both cases, the oxygen exchange is not significant in the evaluated temperature range for the WGS reaction, that is from 200 to 350 °C. The CeP400 support does not exchange oxygen in all the temperature range evaluated, which indicates no mobility of the oxygen atoms of the support. This result is consistent with the description of the rhabdophane-type phase of $CePO_4$, where the oxygen atoms are stabilized forming the structural channels typical of this phase [25]. However, the solid CeP600 exchanges oxygen from 400 °C, reaching a number of exchanged atoms (N_e) equal to 1.5 x 10^{21} atoms per gram of support at 600 °C, which corresponds to a 15% of the total number of atoms present in the solid. Considering that in the monazite-type phase of $CePO_4$ the oxygen atoms are not stabilized forming channels, the mobility of oxygen is expected to increase with respect to the rhabdophane-type phase, in good agreement with the obtained results.

Nevertheless, these results point out the low oxygen mobility in both $CePO_4$ supports, in contrast to the results previously reported for CeO_2 [26-27], in which the totality of the surface oxygen atoms are exchanged at 400°C. The presence of oxygen vacancies associated to the CeO_2 redox properties, that is the presence of the Ce^{3+}/Ce^{4+} redox pair, has demonstrated to play a substantial role regarding the oxygen mobility in this solid, which influences the behavior and reaction mechanism of CeO_2-based catalysts during the WGS reaction [4, 28-29]. In our case, the low oxygen mobility is explained by the great stability of the Ce^{3+} ion in both $CePO_4$ structures [27] previously demonstrated by XPS [8, 30], thus excluding the redox role in these supports.

The same experiment was performed on the corresponding Pt catalysts, in order to determine if the presence of the metal induces changes in the exchange capacity of the solids. Results are shown in Figure 3.

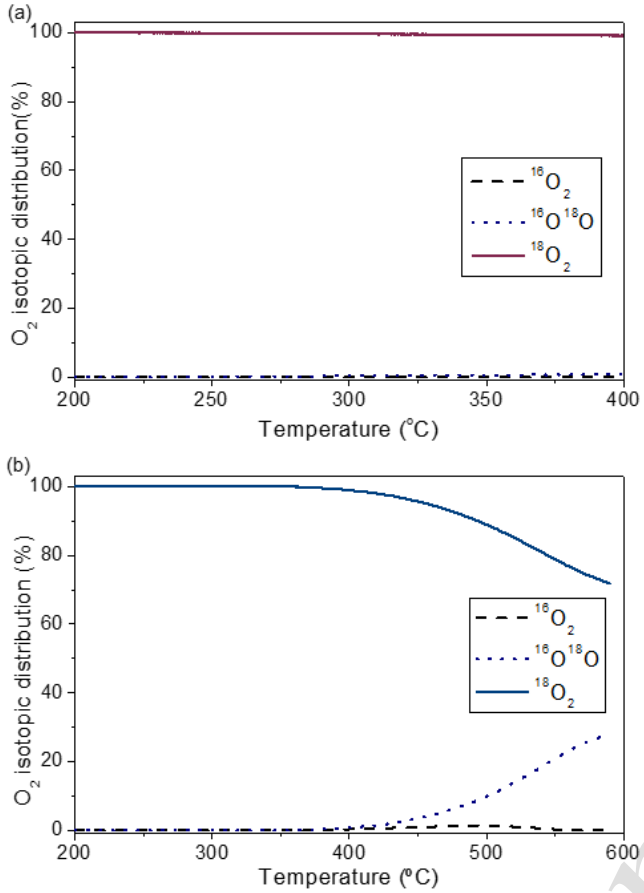

Figure 3. O_2 isotopic distribution (%) as a function of the temperature during temperature-programmed isotopic exchange reaction over (a) Pt/CeP400, (b) Pt/CeP600

Results obtained for the Pt/CeP400 catalyst do not show any difference with respect to the support. In the temperature range evaluated, no exchange occurs, indicating that the presence of Pt does not influence the exchange capacity of the CeP400 support. Although Pt is expected to activate and dissociate the oxygen molecule, which could be reflected in the oxygen isotopic exchange results, previous works [31-32] have proved that highly dispersed Pt particles present lower oxygen activation and dissociation capacity than Pt particles with bigger sizes, which could explain the obtained results, considering the dispersion values reported for the Pt/CeP400 catalyst [8] (Supporting information, **Table S1**).

Regarding the Pt/CeP600 catalyst, the exchange starts at the same temperature than in the corresponding support, that is 400 °C, and the number of oxygen exchanged atoms at 600 °C corresponds to a 13% of the total oxygen atoms present in the support, thus being similar to that value observed for the support. However, the major species observed during the experiment is $^{16}O^{18}O$ being the production of $^{16}O_2$ almost insignificant. As previously mentioned, the presence of Pt is expected to increase the oxygen dissociation capacity. Thus, if $^{18}O_2$ dissociates into two ^{18}O adsorbed atoms on a catalyst containing principally ^{16}O, the formation of $^{16}O^{18}O$ is expected [31] in good agreement with the obtained results. This indicates that contrary to the results obtained for Pt/CeP400, the exchange of oxygen species in the CeP600 support is influenced by the presence of Pt, presumably located in the nearby vicinity of the lattice oxygen ions and OH groups [33]. The oxygen dissociation capacity of the Pt particles in this solid is in good agreement with its lower Pt dispersion value compared to the Pt/CeP400 catalyst [8].

These results allow to confirm the lack of influence of oxygen vacancies in the WGS temperature range where the solids were tested, in good agreement with the lack of the Ce^{3+}/Ce^{4+} redox pair. Since Pt does not allow to improve the exchange activity, it can be concluded that the rate limiting step is the incorporation or the mobility of oxygen atoms in the $CePO_4$ lattice. Consequently, the redox mechanism proposed for the WGS reaction, which implies the existence of oxidation-reduction cycles and the participation of the support oxygen atoms [4, 34-35] can be discarded or have poor influence in this type of solids.

3.2. Isothermal $C^{18}O_2/C^{16}O_2$ Isotopic Exchange

Contrary to the results obtained using $^{18}O_2$, $CePO_4$ supports and Pt catalysts demonstrated to be highly active oxygen exchange materials when using $C^{18}O_2$ as labelled molecule. Figure 4 shows the evolution of the CO_2 isotopic distribution at 300 °C for the $CePO_4$ supports.

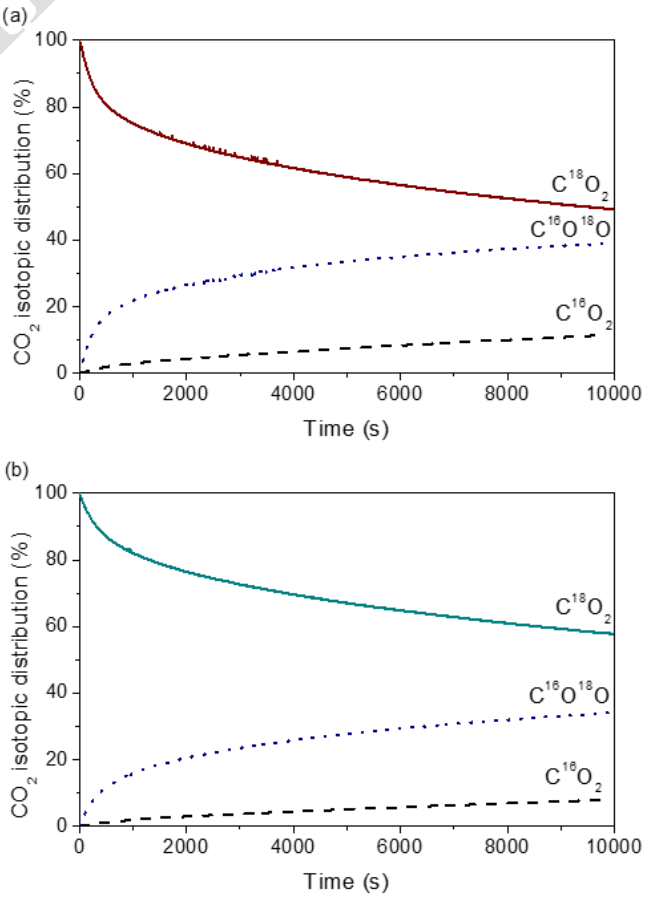

Figure 4. CO_2 isotopic distribution (%) as a function of the time during isotopic exchange reaction at 300 °C over (a) CeP400, (b) CeP600

The oxygen exchange using $C^{18}O_2$ occurs at a high rate, giving rise firstly to the formation of $C^{16}O^{18}O$, followed by the generation of $C^{16}O_2$. Consequently, the mechanism of the $C^{18}O_2$ exchange reaction in both supports proceeds through two consecutive simple exchange mechanisms *via* transfer of one oxygen atom in every stage, as expressed by equation (5):

$$C^{18}O_{2(g)} + {}^{16}O_{(s)} \leftrightarrow C^{16}O^{18}O_{(g)} + {}^{18}O_{(s)} \qquad (5a)$$

$$C^{16}O^{18}O_{(g)} + {}^{16}O_{(s)} \leftrightarrow C^{16}O_{2(g)} + {}^{18}O_{(s)} \qquad (5b)$$

The second step involving the formation of $C^{16}O_2$ takes place almost instantly to the first one, which demonstrates a fast activation of CO_2 on the supports. Nevertheless, although the initial rate of exchange (corresponding to the exchange of oxygen surface atoms) is high, long times are required to reach the equilibrium, pointing out that the exchange with the bulk oxygen atoms is hindered.

Similar results were obtained for the Pt catalysts, as shown in Figure 5. The exchange mechanism was the same than that observed in the supports, and by the same token the exchange demonstrated to be very fast at the beginning of the exchange reaction, taking long times to reach the equilibrium. The little effect of Pt addition regarding oxygen exchange suggests that $C^{18}O_2$ exchange takes place mainly on the supports through a direct process [22].

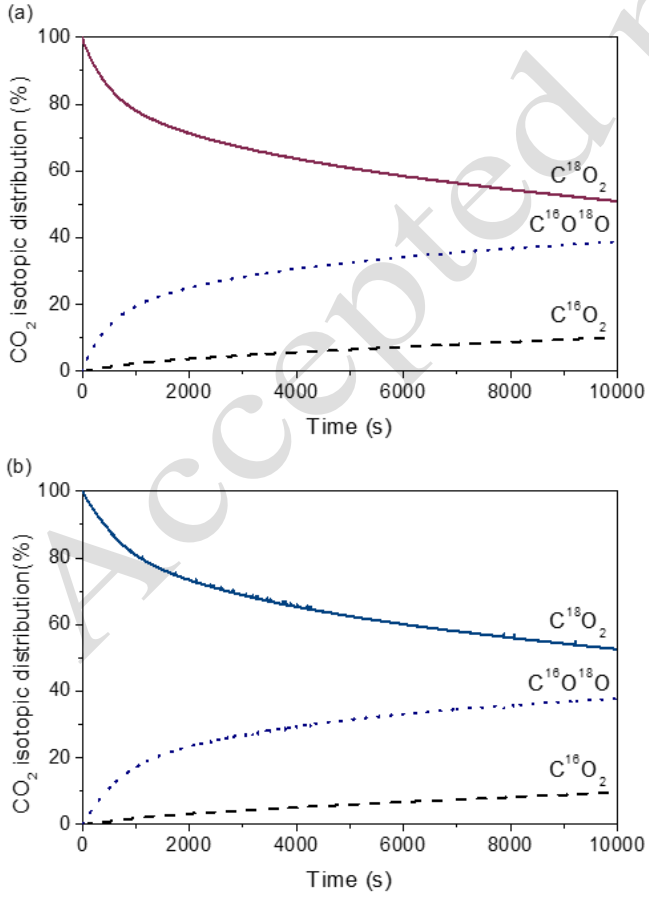

Figure 5. CO_2 isotopic distribution (%) as a function of the time during isotopic exchange reaction at 300 °C over (a) Pt/CeP400, (b) Pt/CeP600

In order to compare the oxygen mobility in every solid, the number of oxygen exchanged atoms (N_e) as a function of the time is presented in Figure 6. Additionally, N_e data after two hours of reaction and R_e are summarized in Table 1.

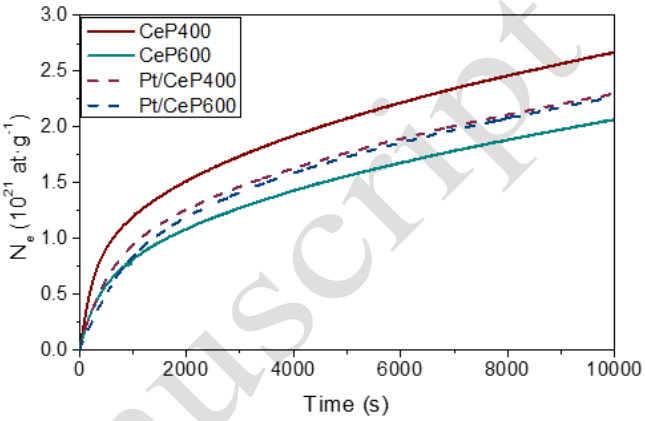

Figure 6. Ne evolution as a function of the time for the CePO4 supports and Pt catalysts

Table 1. Number of oxygen exchanged atoms (N_e) and $C^{18}O_2$ rates of exchange (R_e) of the $CePO_4$ supports and Pt catalysts at 300 °C

Sample	N_e (10^{21} at·g^{-1})	R_e (10^{18} at·g^{-1}·s^{-1})
CeP400	2.7	4.6
CeP600	2.0	2.7
Pt/CeP400	2.3	2.6
Pt/CeP600	2.3	2.0

Results demonstrate that the activation of the CO_2 molecule in the solids surface is not a limiting process, contrary to the activation of the O_2 molecule. Regarding the supports, both N_e and R_e values are superior for CeP400, exposing its greater CO_2 activation capacity. Whereas CeP400 support exchanges a 24% of the total atoms present in the solid, CeP600 exchanges a 20% of its atoms.

Nevertheless, in the presence of Pt N_e values become similar for both solids, although the Pt/CeP400 catalyst presents a slightly superior exchange capacity, particularly at the beginning of the reaction. According to the data after two hours of reaction (Table 1), both N_e and R_e values for the Pt/CeP400 catalyst are lower than those of the CeP400 support. Additionally, the number of oxygen exchanged atoms in such catalyst corresponds to a 21% of the total atoms present in the solid, very close to the 22% exchanged in the Pt/CeP600 catalyst. Consequently, the presence of Pt induces a negative effect on the oxygen exchange capacity of the CeP400 support, especially marked during the exchange reaction with the bulk oxygen atoms.

Considering the long times required to reach the equilibrium in both the supports and catalysts, the calculation of the diffusion coefficient using Kakioka's model results of great interest [23-24]. In order to calculate the oxygen diffusion coefficient, it is necessary to distinguish (1) the exchange with the surface oxygen atoms, which takes place at a high rate with the oxygen atoms of CO_2 and (2) the exchange with the bulk oxygen, determined by the diffusion rate in the inside of the solid. Thus, such model has to be applied once the fast oxygen exchange with the surface atoms has taken place. Linear fitting of the results and diffusion coefficient values are displayed in Figure 7 and Table 2, respectively.

Diffusion coefficient of the CeP400 support is smaller than that of CeP600, which could be related to a hindered oxygen diffusion in the former due to the presence of channels in its structure. In the presence of Pt, no significant differences are observed between CeP600 and Pt/CeP600, thus denoting no influence of the metal particles during the diffusion processes. On the contrary, the diffusion coefficient of Pt/CeP400 decreases significantly with respect to CeP400. In our previous work [8], TEM micrographs suggested the arrangement of some Pt particles inside the channels of CeP400, thus the presence of Pt both on the surface and in such cavities could hinder the diffusion of oxygen in the bulk of the CeP400 support (Supporting information, **Figure S2**).

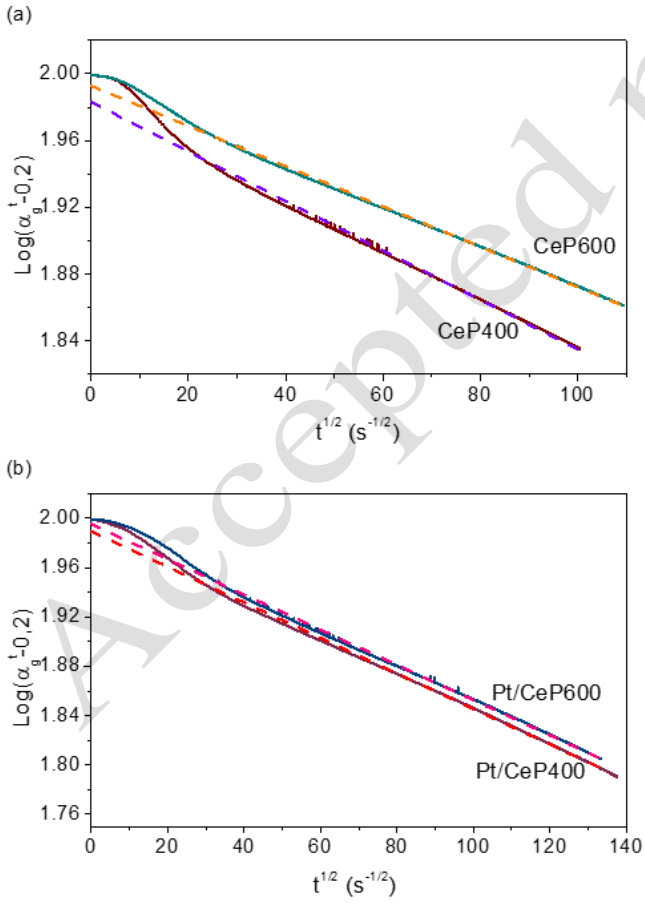

Figure 7. Linear fitting using Kakioka's model from $C^{18}O_2$ isotopic exchange results at 300 °C over (a) $CePO_4$ supports, (b) Pt catalysts

Table 2. Diffusion coefficient (D) of the CePO4 supports and Pt catalysts calculated by Kakioka's model

Sample	D (10^{-22} $m^2 \cdot s^{-1}$)
CeP400	1.47
CeP600	4.41
Pt/CeP400	0.86
Pt/CeP600	4.93

The obtained results demonstrate a high oxygen mobility in the solids using $C^{18}O_2$, which implies the formation and decomposition of carbonate-like intermediates and thus, suggesting that the WGS *associative* mechanism could be the preferred path in these solids.

3.3. *Operando* DRIFTS study of the WGS reaction mechanism

$^{18}O_2$ isotopic exchange results have demonstrated that both the $CePO_4$ supports and Pt catalysts present no activity towards oxygen exchange in the WGS temperature range evaluated in our samples (200-350 °C), which discards the participation of oxygen vacancies in these solids and thus suggests a poor influence of the so-called WGS *redox* mechanism. On the contrary, the great oxygen exchange activity using $C^{18}O_2$ suggests a preference for the WGS *associative* mechanism in these solids.

In order to elucidate the WGS reaction mechanism taking place in these solids, *operando* DRIFTS experiments were performed under WGS reaction atmosphere. Difference spectra during the reaction at each temperature were obtained by subtraction of the spectra of the samples before the introduction of the reaction mixture.

Difference spectra of the Pt/CeP400 catalyst when subjected to the reaction mixture (4.5% CO, 10% H_2O, Ar balance) are shown in Figure 8. Results reveal the presence of adsorbed water even at relatively high temperature as observed in previous experiments [8], in agreement with the appearance of bands at 1625 cm^{-1}, corresponding to the H-O-H bending mode of hydrogen-bonded water, and those in the 3100-3500 cm^{-1} range, attributed to surface-bonded water [36]. Bands in the 5100-5300 cm^{-1} range, ascribed to the overtones of the water stretching vibrations, allow to confirm the presence of molecular water [37], Figure 8(a).

Additionally, bands corresponding to linear-bonded CO, generally found between 2000-2100 cm^{-1}, appear at 2055, 2073 and 2080 cm^{-1}, as shown in Figure 8(b). The presence of these contributions exposes different environments of the Pt particles in the Pt/CeP400 solid. The shifts of the CO stretching frequency could be explained by several reasons, as changes in the Pt exposed faces or changes in the electron density of the metal particles induced by the support, which affects the number of available electrons for back-bonding

to the CO π* orbitals [38-39]. In our case, these bands have been assigned to CO linearly adsorbed on different adsorption sites of platinum crystallites possessing surface atoms with different coordination. Greenler et al. [40] obtained similar features during CO adsorption on Pt/SiO_2 catalysts. They reported three bands at 2063, 2070 and 2081 cm^{-1}, ascribed to CO linearly adsorbed on corner, edge and face atoms of Pt crystallites, respectively. Furthermore, a shoulder at about 2010 cm^{-1} is observed in our spectra, which has been ascribed to CO linearly adsorbed on a weakly coordinated Pt atom. According to Bazin and co-workers [41], the origin of this Pt site could be a Pt coordination site located onto steps or kinks of small particles or correspond to CO linearly adsorbed on very small Pt particles. An additional band at very low frequency (1965 cm^{-1}) is also observed, which have been tentatively attributed to CO linearly adsorbed on the Pt species occluded in the channels of the rhabdophane-type phase. The CeP400 channels are constituted by oxygen atoms which present local negative charge, being able to donate electron density to the adjacent Pt atoms. Thus, the increased Pt electron density could provoke an increased bonding to the CO π* orbitals, decreasing the CO stretching frequency. This result is in accordance with previous works, where a contribution at *ca.* 1970 cm^{-1} has been observed in the spectra of Pt catalysts supported on zeolites, being attributed to CO linearly adsorbed on Pt located on the zeolite cages [38-39].

As a consequence of the interaction between the reactants, surface carbonaceous species are formed, according to the contributions emerging at 1370, 1381, 1589 and 2850 cm^{-1} (Figure 8(a) and (c)). These features seem to indicate the formation of formate ($HCOO^-$) species. The bands at 1589 and 1370 cm^{-1} have been assigned to the asymmetric and symmetric CO stretching vibrations (ν_{as} CO and ν_s CO), respectively, whereas the bands at 2850 and 1381 cm^{-1} have been attributed to the CH stretching (νCH) and CH bending (δCH) vibrations, respectively. In order to identify the type of coordination of the formate species, a general procedure consists on the evaluation of the splitting between the CO asymmetric and symmetric stretching modes, $\Delta\nu_{as\text{-}s}$ [42-44]. In this case, the splitting is not representative of the typical coordination structures described for surface formate species. This could be explained by the formation of hydrogen bonds, since fields due to water molecules can affect the splitting value [44-45]. Miao et al. obtained similar bands in Pt/apatite catalysts [6], which were attributed to formate ions in aqueous solution [46] and icy matter [47]. Furthermore, the broad band at about 1770 cm^{-1}, also present in our spectra, agrees with the value reported for the CO stretching mode (νCO) of gaseous formic acid [48], which is produced by means of the reaction between CO and H_2O. Canepa et al. [49] carried out an *ab initio* study on the interaction of formic acid with hydroxyapatite surfaces, which explained properly the WGS intermediates observed by Miao et al. [6] in Pt/apatite catalysts. According to their results, CO and H_2O react to produce formic acid, which can adsorb molecularly on the (001) surface. However, the acid dissociates spontaneously in the water-reconstructed (010) surface to produce formate species, which are the WGS reaction intermediates. Thus, in our Pt/CeP400 catalyst, the adsorption of formic acid could take place in those surfaces presenting less affinity by water, whereas the formate species appear in the water-enriched surface of CeP400.

On the other hand, Lustemberg et al. [50] studied several coordination modes of formate species, considering both the Δν values and the position of the vibration bands. According to these authors, the CO asymmetric and symmetric stretching vibrations of bidentate formate species appear at 1550 and 1371 cm^{-1}, respectively ($\Delta\nu$=179 cm^{-1}). In our case, these bands are found at 1589 and 1370 cm^{-1} ($\Delta\nu$=218 cm^{-1}), suggesting the presence of bidentate formate species in the surface of the Pt/CeP400 catalyst.

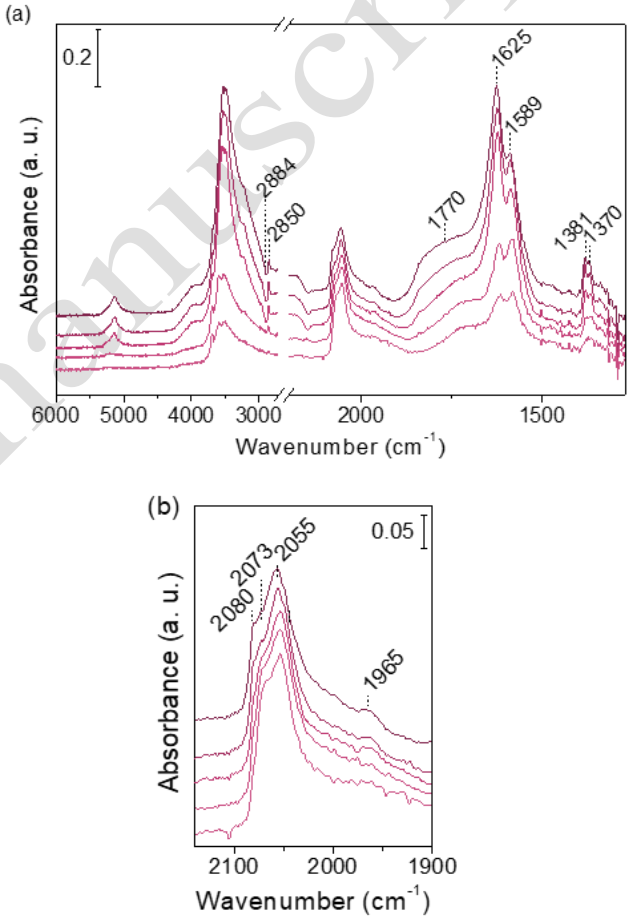

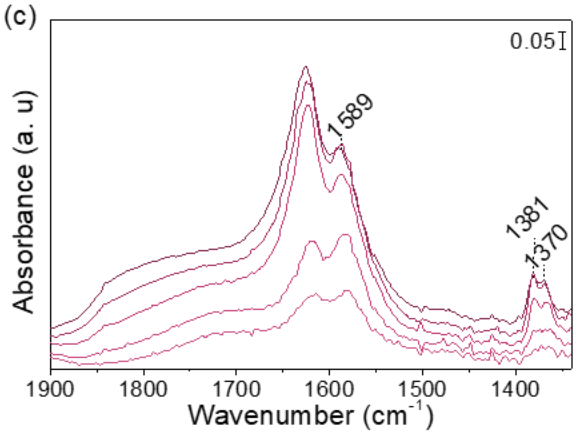

Figure 8. (a) Difference spectra (general) of the Pt/CeP400 catalyst under WGS reaction flow, and enlargement of (b) 2200-1900 cm^{-1} and (c) 1900-1340 cm^{-1} range, from 150 (top) to 350 °C (bottom).

Difference spectra of the Pt/CeP600 catalyst are shown in Figure 9. As for the Pt/CeP400 catalyst, bands ascribed to adsorbed water at 1622 cm^{-1} and in the 3100-3500 cm^{-1} region appear (Figure 9(a)), although their intensity are lower than those of the Pt/CeP400 catalysts, in accordance with the lowest water adsorption capacity of the support CeP600 [8]. Furthermore, the band in the 5100-5300 cm^{-1} range observed for the Pt/CeP400 catalyst does not appear in the spectra of this solid, indicating the absence of a water layer in which the formate species could be dissolved.

Bands attributed to linear Pt^0-CO are observed in the 2000-2100 cm^{-1} range (Figure 9(b)). Differently from the Pt/CeP400 solid, only two bands at 2057 and 2076 cm^{-1} are observed, pointing out the lower number of coordination environments of the Pt particles in Pt/CeP600. Such bands correspond to CO linearly adsorbed on corner and edge atoms of Pt crystallites [40], respectively. As for the spectra of the Pt/CeP400 catalyst, a shoulder at about 2010 cm^{-1} is present, attributed to CO linearly adsorbed on a weakly coordinated Pt atom [41]. Furthermore, the band at 1965 cm^{-1} present in the Pt/CeP400 spectra is not observed in this catalyst, reinforcing the assignment of this contribution to Pt particles located in the rhabdophane-type phase structural channels.

As a result of the interaction between reactants, bands corresponding to bidentate formate groups are present at 1370, 1381, 1588 and 2843 cm^{-1} (Figure 9(a) and (c)), similarly to the results obtained for Pt/CeP400. The contributions at 1588 and 1370 cm^{-1} have been attributed to the asymmetric and symmetric stretching vibrations of the CO group (ν_{as} CO and ν_s CO), whereas the bands at 2843 and 1381 cm^{-1} have been ascribed to the CH stretching (νCH) and CH bending (δCH) vibrations. However, a second type of formate species is present, according to the bands at 1337, 1362, 1564 and 2976 cm^{-1}. As reported by Lustemberg et al. [50], ν(CO) asymmetric and symmetric modes of monodentate formates are observed at 1580 and 1335 cm^{-1} ($\Delta\nu$=245 cm^{-1}). In our case, $\Delta\nu$ is 227 cm^{-1}. Therefore, we can conclude that in this solid, the lower amount of water favours the stabilization of monodentate formate species.

In addition, a weak band at 1478 cm^{-1} points out the simultaneous formation of carbonate species.

Whatever the catalyst, no new –OH groups resulting from the interaction of the water molecule with the oxygen vacancies of the supports appear during the WGS reaction, which is in good agreement with the absence of oxygen exchange in these solids demonstrated by $^{18}O_2$ isotopic exchange experiments. Consequently, the WGS *redox* mechanism can be discarded in this type of solids.

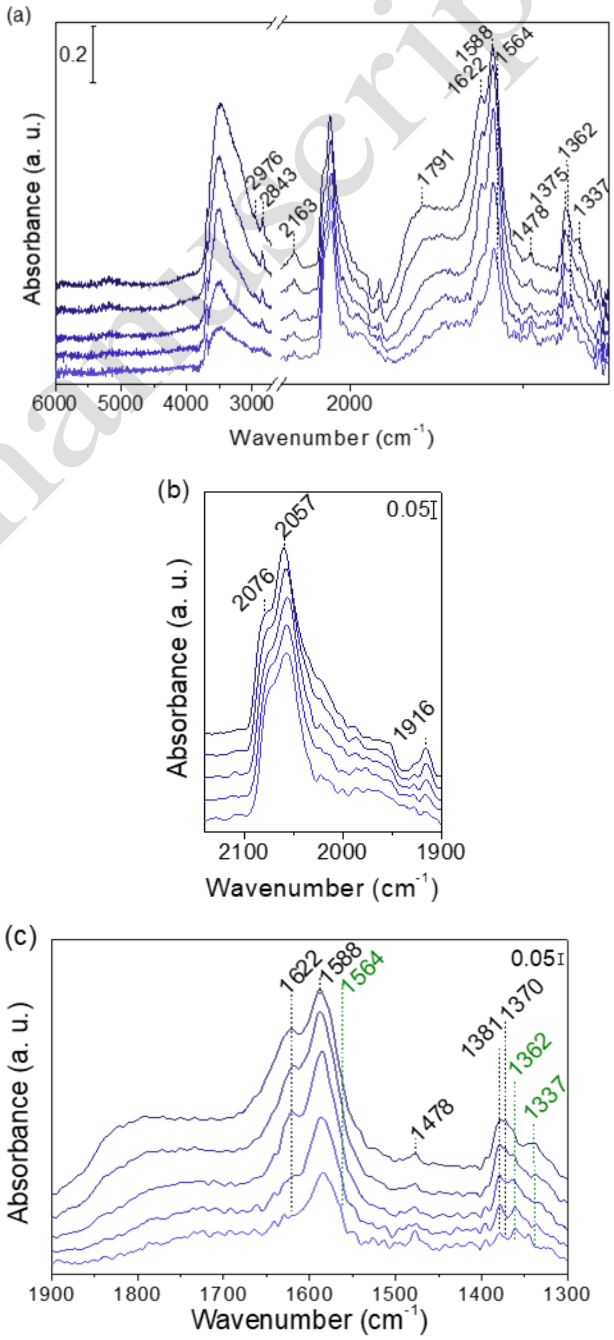

Figure 9. (a) Difference spectra (general) of the Pt/CeP600 catalyst under WGS reaction flow, and enlargement of (b) 2200-1900 cm^{-1} and (c) 1900-1300 cm^{-1} range, from 150 (top) to 350 °C (bottom)

According to the previously mentioned results, only bidentate formate species are formed on the surface of the Pt/CeP400 catalyst, whereas bidentate and monodentate species are observed in Pt/CeP600. Jacobs et al. [51] studied the WGS reaction mechanism on a Pt/CeO_2 catalyst after a pre-treatment under H_2. They demonstrated that the partial reduction of ceria leads to the formation of geminal OH groups, which react with CO to form bidentate formate species, the active intermediate species during the WGS reaction. However, some authors claim that formate species act as spectators during the WGS reaction, being carboxyl species the true intermediates [52].

In order to clarify the role of the bidentate formates in our catalysts, the evolution of the ~2850 cm^{-1} band intensity was compared to the CO_2 production rate as a function of the temperature. In the case of the Pt/CeP600 catalyst, the intensity of the bands at 2976 and 1478 cm^{-1} attributed to monodentate formate and carbonate species, respectively, are also evaluated. Results are shown in Figure 10.

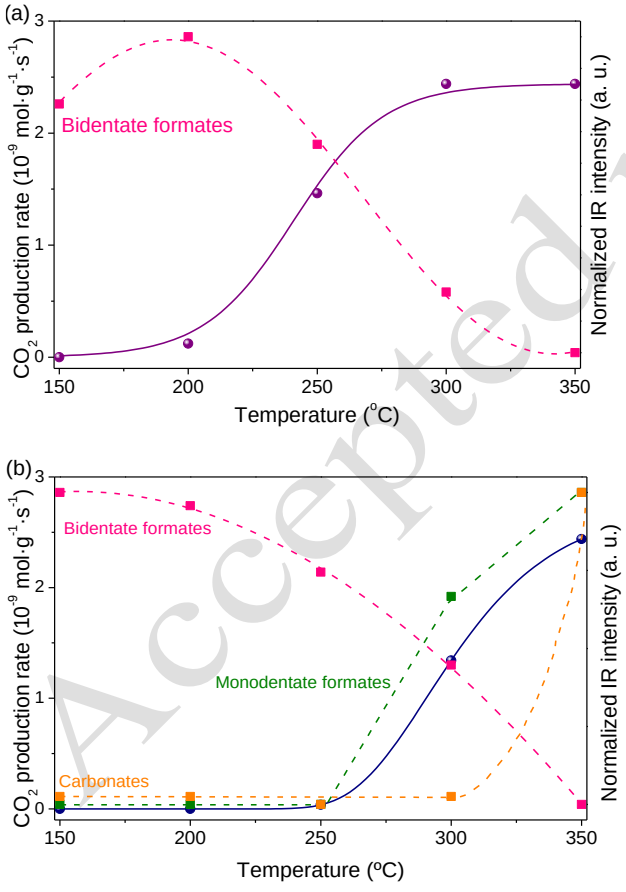

Figure 10. Comparison between the CO_2 production during *operando* DRIFTS experiments (continuous line) and the evolution of the main IR band for the detected carbonaceous species (dashed lines) for (a) Pt/CeP400 and (b) Pt/CeP600 catalysts.

Results demonstrate a greater catalytic performance of Pt/CeP400 with respect to Pt/CeP600, in good agreement with the catalytic activity tests (Supporting Information, **Figure S1**).

For both catalysts, an initial increase of the bidentate formate band intensity takes place between 150 and 200 °C, at low CO conversion values. As the temperature increases, CO_2 production increases and the bidentate formate band intensity decreases to the same extent, suggesting that bidentate formates are the intermediate species in both catalysts. This has been confirmed by comparing the CO_2 production registered during the experiment and the ~2850 cm^{-1} band intensity as a function of the time, which shows that both the increase in the CO_2 production and the decrease in the band intensity present the same slope with opposite signs in all the temperature range evaluated, thus confirming that CO_2 formation is the result of the decomposition of the bidentate formate species.

Regarding Pt/CeP600, the formation of surface carbonate species could take place through two possible mechanisms [53]: 1) the interaction of the produced CO_2 with the oxygen atoms of the support, in which case the drop of the formates band intensity must initiate before the formation of carbonates, or 2) the oxidation of the formate species by the available surface oxygen to yield carbonate. In this case, carbonates formation should start simultaneously to formates consumption. Thus, according to our results, the formation of surface carbonates results from the interaction of CO_2 with the CeP600 support. According to Hilaire and co-workers [54], carbonate is stable in reduced CeO_2, where cerium is present as Ce^{3+} similarly to the $CePO_4$ supports. However, carbonate species are easily decomposed by oxidation with H_2O. Consequently, the stabilization of carbonates on the Pt/CeP600 surface could be explained by the lower water retention capacity of CeP600 with respect to CeP400. Since water is available on the surface of the latter even at 350 °C, the decomposition of the carbonate species could take place, increasing reaction rates [54]. The trend followed by the carbonates and monodentate formates bands in Pt/CeP600 indicates that the concentration of both species increases along the WGS reaction. Hence, both carbonate and monodentate formate species may have a spectator or catalytic poisoning role, contributing to the blocking of the active sites and thus, explaining its lower catalytic performance with respect to Pt/CeP400.

Consequently, results suggest that the WGS reaction in both catalysts proceed *via* an associative mechanism through the generation of formate species, according to the following scheme:

$$CO_{(g)} + H_2O_{(g)} \leftrightarrow CO^* + OH^* + H^* \leftrightarrow HCOO^* + H^* \leftrightarrow CO_2^* + 2H^* \leftrightarrow CO_{2(g)} + H_{2(g)}$$

Where the asterisk (*) implies that the corresponding species is adsorbed.

Considering this reaction scheme, which implies the dissociation of the water molecule into OH and H species and taking into account that the $CePO_4$ supports do not dissociate the water molecule [8], it could be concluded that the OH

and H species participating in the formate generation are those produced by the dissociation of the water molecule on the Pt particles. Phatak et al. [55] developed an interesting DFT investigation on the adsorption and dissociation steps of water on different metals, relating them to the WGS reaction mechanism. In every case, water dissociation occurs by means of the following 2 steps:

$H_2O^* + * \rightarrow OH^* + H^*$ (1)

$OH^* + * \rightarrow O^* + H^*$ (2)

In the case of Pt, the activation energy barrier for OH dissociation is larger than that for the abstraction of the first H atom in the H_2O molecule. Accordingly, in WGS conditions, atomic H is the most abundant surface intermediate, followed by OH and finally, O. These results are in agreement with the reaction mechanism observed in Pt/CeP400. However, the observation of the Pt-H vibration is difficult, since it appears in the same region than the Pt-CO one [56]. Likewise, the observation of the Pt-OH vibration results difficult in the presence of H_2O, since it appears in the 3600-3400 cm^{-1} range, where the broad contributions ascribed to OH groups of bonded water are also present, thus obscuring this region [57].

According to DRIFTS results, the WGS reaction in these solids occurs through a bidentate formate-mediated mechanism. Since $CePO_4$ supports do not present the capacity of dissociating the water molecule, the water dissociation step is carried out in the Pt particles, as well as the adsorption of CO. Consequently, the formation of bidentate formate species seems to take place on the metal phase. Furthermore, Pt has demonstrated to promote H-transfer by assisting the hydrogen abstraction from the formate intermediate and a neighboring OH group, allowing H_2 recombination and desorption from the catalyst surface, whereas the presence of H_2O lowers the activation energy of formate decomposition and changes the selectivity to favor formate dehydrogenation over dehydration [58-59]. Therefore, the metal-support interface could have an important function regarding the decomposition of the formate species. Whereas the role of the $CePO_4$ supports is to supply H_2O in the vicinity of Pt during the WGS reaction, Pt particles could as well assist the decomposition of the formate species to generate the reaction products. The higher H_2O content in the CeP400 surface could facilitate formates decomposition to a greater extent, thus explaining the higher WGS catalytic performance of the Pt/CeP400 catalyst.

4. CONCLUSIONS

Oxygen mobility in the rhabdophane (CeP400) and monazite-type (CeP600) phases of $CePO_4$ and the corresponding Pt catalysts has been evaluated by $^{18}O_2/^{16}O_2$ and $C^{18}O_2/C^{16}O_2$ isotopic exchange experiments. Every solid present poor oxygen exchange capacity using $^{18}O_2$ as labelled molecule, pointing out the absence of oxygen vacancies able to participate in the WGS reaction and thus, suggesting a poor influence of the WGS *redox* mechanism. On the contrary, the evaluated solids present high oxygen exchange capacity using $C^{18}O_2$, indicating that the formation and decomposition of carbonate-like intermediates can occur in the solids surface and, consequently, suggesting the WGS *associative* mechanism as the main path in these catalytic systems. *Operando* DRIFTS results confirm that the WGS reaction occurs through an *associative* mechanism *via* bidentate formate intermediate species, whereas no formation of new –OH groups is observed, ruling out the *redox* mechanism, in good agreement with the isotopic exchange results.

The greater catalytic activity of the Pt/CeP400 catalyst is explained by the formation of only bidentate formate species in the catalyst surface, which are proposed as the active species during the WGS reaction. On the contrary, the lower surface water content in the Pt/CeP600 catalyst gives rise to the additional formation of monodentate formate and carbonate species, which could block the active sites and provoke a decrease on the catalytic performance.

ASSOCIATED CONTENT

Supporting Information

WGS catalytic performance of the Pt catalysts, mean Pt particle size and metal dispersion values, TEM micrographs.

This material is available free of charge via the Internet at http://pubs.acs.org.

AUTHOR INFORMATION

Corresponding Author

* Sara Navarro-Jaén

Present Addresses

† Sara Navarro-Jaén. Univ. Lille, CNRS, Centrale Lille, ENSCL, Univ. Artois, UMR 8181, UCCS, Unité de Catalyse et Chimie du Solide, F-59000, Lille, France. Current e-mail address: sara.navarro-jaen@univ-lille.fr

Oscar H. Laguna. Departamento de Ingeniería Química, Medioambiental y de los Materiales. Campus Científico Tecnológico de Linares- Universidad de Jaén. Av. De la Universidad, s/n, 23700 Linares (Jaén), Spain

Author Contributions

The manuscript was written through contributions of all authors. All authors have given approval to the final version of the manuscript.

Notes

The authors declare no conflict of interest.

ACKNOWLEDGMENT

The work presented in this manuscript is reproduced in part from: Navarro-Jaén, S., Phosphate-based catalysts for the WGS reaction: synthesis, reactivity and mechanistic considerations. Ph.D. Thesis, University of Seville, January 2019.

The authors acknowledge the financial support of the Spanish Ministry of Economy and Competitiveness through the Project ENE2015-66975-C3-2-R.

S. Navarro-Jaén is thankful for the financial support provided by the Erasmus+ Mobility Agreement between the University of Seville and the University of Poitiers.

REFERENCES

1. Song, C., Fuel processing for low-temperature and high-temperature fuel cells: Challenges and opportunities for sustainable development in the 21st century. *Catal. Today* **2002,** *77*, 17-49.
2. Ilieva, L.; Tabakova, T.; Pantaleo, G.; Ivanov, I.; Zanella, R.; Paneva, D.; Velinov, N.; Sobczak, J. W.; Lisowski, W.; Avdeev, G.; Venezia, A. M., Nano-gold catalysts on Fe-modified ceria for pure hydrogen production via WGS and PROX: Effect of preparation method and Fe-doping on the structural and catalytic properties. *Appl. Catal., A* **2013,** *467*, 76-90.
3. Gonzalez Castaño, M.; Reina, T. R.; Ivanova, S.; Centeno, M. A.; Odriozola, J. A., Pt vs. Au in water–gas shift reaction. *J. Catal.* **2014,** *314*, 1-9.
4. Vecchietti, J.; Bonivardi, A.; Xu, W.; Stacchiola, D.; Delgado, J. J.; Calatayud, M.; Collins, S. E., Understanding the Role of Oxygen Vacancies in the Water Gas Shift Reaction on Ceria-Supported Platinum Catalysts. *ACS Catal.* **2014,** *4*, 2088-2096.
5. Miao, D.; Cavusoglu, G.; Lichtenberg, H.; Yu, J.; Xu, H.; Grunwaldt, J.-D.; Goldbach, A., Water-gas shift reaction over platinum/strontium apatite catalysts. *Appl. Catal., B* **2017,** *202*, 587-596.
6. Miao, D.; Goldbach, A.; Xu, H., Platinum/Apatite Water-Gas Shift Catalysts. *ACS Catal.* **2016,** *6*, 775-783.
7. Navarro-Jaén, S.; Romero-Sarria, F.; Centeno, M. A.; Laguna, O. H.; Odriozola, J. A., Phosphate-type supports for the design of WGS catalysts. *Appl. Catal., B* **2019,** *244*, 853-862.
8. Navarro-Jaén, S.; Centeno, M. Á.; Laguna, O. H.; Odriozola, J. A., Pt/$CePO_4$ catalysts for the WGS reaction: influence of the water-supplier role of the support on the catalytic performance. *J. Mater. Chem. A* **2018,** *6*, 17001-17010.
9. Kalamaras, C. M.; Dionysiou, D. D.; Efstathiou, A. M., Mechanistic Studies of the Water–Gas Shift Reaction over Pt/$Ce_xZr_{1-x}O_2$ Catalysts: The Effect of Pt Particle Size and Zr Dopant. *ACS Catal.* **2012,** *2*, 2729-2742.
10. Gokhale, A. A.; Dumesic, J. A.; Mavrikakis, M., On the mechanism of low temperature water gas shift reaction on copper. *J. Am. Chem. Soc.* **2008,** *130*, 1402-1414.
11. Choi, S.; Sang, B. I.; Hong, J.; Yoon, K. J.; Son, J. W.; Lee, J. H.; Kim, B. K.; Kim, H., Catalytic behavior of metal catalysts in high-temperature RWGS reaction: In-situ FT-IR experiments and first-principles calculations. *Sci. Rep.* **2017,** *7*, 41207.
12. Fu, Q.; Saltsburg, H.; Flytzani-Stephanopoulos, M., Active Nonmetallic Au and Pt Species on Ceria-Based Water-Gas Shift Catalysts. *Science* **2003,** *301*, 935-938.
13. Ratnasamy, C.; Wagner, J. P., Water Gas Shift Catalysis. *Catal. Rev.* **2009,** *51*, 325-440.
14. Olympiou, G. C.; Kalamaras, C. M.; Zeinalipour-Yazdi, C. D.; Efstathiou, A. M., Mechanistic aspects of the water-gas shift reaction on alumina-supported noble metal catalysts: in situ DRIFTS and SSITKA-mass spectrometry studies. *Catal. Today* **2007,** *127*, 304-318.
15. Byron, S. R. J.; Loganathan, M.; Shanthaz, M. S., A Review of the Water Gas Shift Reaction Kinetics. *Int. J. Chem. React. Eng.* **2010,** *8*, 1-32.
16. Reddy, G. K.; Smirniotis, P. G., *Water Gas Shift Reaction: Research Developments and Applications*. Elsevier: Amsterdam, The Netherlands, 2015.
17. Jain, R.; Poyraz, A. S.; Gamliel, D. P.; Valla, J.; Suib, S. L.; Maric, R., Comparative study for low temperature water-gas shift reaction on Pt/ceria catalysts: Role of different ceria supports. *Appl. Catal., A* **2015,** *507*, 1-13.
18. Maciel, C. G.; Silva, T. d. F.; Assaf, E. M.; Assaf, J. M., Hydrogen production and purification from the water–gas shift reaction on $CuO/CeO_2–TiO_2$ catalysts. *Appl. Energy* **2013,** *112*, 52-59.
19. Maupin, I.; Mijoin, J.; Belin, T.; Morais, C.; Montouillout, V.; Duprez, D.; Bion, N., Direct evidence of the role of dispersed ceria on the activation of oxygen in NaX zeolite by coupling the $^{17}O/^{16}O$ isotopic exchange and ^{17}O solid-state NMR. *J. Catal.* **2013,** *300*, 136-140.
20. Yang, W.; Zhang, R.; Chen, B.; Bion, N.; Duprez, D.; Hou, L.; Zhang, H.; Royer, S., Design of nanocrystalline mixed oxides with improved oxygen mobility: a simple non-aqueous route to nano-$LaFeO_3$ and the consequences on the catalytic oxidation performances. *Chem. Commun.* **2013,** *49*, 4923-5.
21. Duprez, D., *Isotopes in Heterogeneous Catalysis*. Imperial College Press: 2006; Vol. 4.
22. Ojala, S.; Bion, N.; Rijo Gomes, S.; Keiski, R. L.; Duprez, D., Isotopic Oxygen Exchange over Pd/Al_2O_3 Catalyst: Study on $C^{18}O_2$ and $^{18}O_2$ Exchange. *ChemCatChem* **2010,** *2*, 527-533.
23. Kakioka, H.; Ducarme, V.; Teichner, S. J., I. Échange isotopique de ^{18}O du gaz carbonique avec les ions oxygène de l'hémipentoxyde de vanadium. *J. Chim. Phys.* **1971,** *68*, 1715-1721.
24. Kakioka, H.; Ducarme, V.; Teichner, S. J., II. Échange isotopique de ^{18}O du gaz carbonique avec les ion oxygène de l'hémipentoxyde de vanadium dopé par l'ion molybdène Mo^{6+}. *J. Chim. Phys.* **1971,** *68*, 1722-1725.
25. Mooney, R. C. L., X-ray Diffraction Study of Cerous Phosphate and Related Crystals. I. Hexagonal modification. *Acta Crystallogr.* **1950,** *3*, 337-340.
26. Madier, Y.; Descorme, C.; Le Govic, A. M.; Duprez, D., Oxygen Mobility in CeO_2 and $Ce_xZr_{(1-x)}O_2$ Compounds: Study by CO Transient Oxidation and $^{18}O/^{16}O$ Isotopic Exchange. *J. Phys. Chem. B* **1999,** *103*, 10999-11006.
27. Larese, C.; Cabello Galisteo, F.; López Granados, M.; Mariscal, R.; Fierro, J. L. G.; Lambrou, P. S.; Efstathiou, A. M., Effects of the $CePO_4$ on the oxygen storage and release properties of CeO_2 and $Ce_{0.8}Zr_{0.2}O_2$ solid solution. *J. Catal.* **2004,** *226*, 443-456.
28. González-Castaño, M.; Reina, T. R.; Ivanova, S.; Martínez Tejada, L. M.; Centeno, M. A.; Odriozola, J. A., O_2-assisted Water Gas Shift reaction over structured Au and Pt catalysts. *Appl. Catal., B* **2016,** *185*, 337-343.
29. Li, Y.; Fu, Q.; Flytzani-Stephanopoulos, M., Low-temperature water-gas shift reaction over Cu- and Ni-loaded cerium oxide catalysts. *Appl. Catal., B* **2000,** *27*, 179-191.
30. Pemba-Mabiala, J. M.; Lenzi, M.; Lenzi, J.; Lebugle, A., XPS Study of Mixed Cerium-Terbium Ortophosphate Catalysts. *Surf. Interface Anal.* **1990,** *15*, 663-667.
31. Holmgrem, A.; Duprez, D.; Andersson, B., A Model of Oxygen Transport in Pt/Ceria catalysts from Isotope Exchange. *J. Catal.* **1999,** *182*, 441-448.
32. Holmgrem, A.; Andersson, B., Oxygen Storage Dynamics in $Pt/CeO_2/Al_2O_3$ Catalysts. *J. Catal.* **1998,** *178*, 14-25.
33. Ducarme, V.; Vedrine, J. C., Study of Surface Atom Behaviour on Pt/SiO_2 and Pt/Al_2O_3 Catalysts by Isotopic Exchange of Oxygen from CO_2. *J. Chem. Soc., Faraday Trans. 1* **1977,** *74*, 506-508.
34. González-Castaño, M.; Ivanova, S.; Ioannides, T.; Centeno, M. A.; Odriozola, J. A., Deep insight into Zr/Fe combination for successful $Pt/CeO_2/Al_2O_3$ WGS catalyst doping. *Catal. Sci. Technol.* **2017,** *7*, 1556-1564.
35. García-Moncada, N.; González-Castaño, M.; Ivanova, S.; Centeno, M. Á.; Romero-Sarria, F.; Odriozola, J. A., New concept for old reaction: Novel WGS catalyst design. *Appl. Catal., B* **2018,** *238*, 1-5.

36. Romero-Sarria, F.; Domínguez, M. I.; Centeno, M. A.; Odriozola, J. A., CO oxidation at low temperature on Au/$CePO_4$: Mechanistic aspects. *Appl. Catal., B* **2011,** *107*, 268-273.

37. Frost, R. L.; Erickson, K. L., Near-infrared spectroscopic study of selected hydrated hydroxylated phosphates. *Spectrochim. Acta, Part A* **2005,** *61* (1-2), 45-50.

38. Kappers, M. J.; van der Maas, J. H., Correlation between CO frequency and Pt coordination number. A DRIFT study on supported Pt catalysts. *Catal. Lett.* **1991,** *10*, 365-374.

39. Lane, G. S.; Miller, J. T.; Modica, F. S.; Barr, M. K., Infrared Spectroscopy of Adsorbed Carbon Monoxide on Platinum/Nonacidic Zeolite Catalysts. *J. Catal.* **1993,** *141*, 465-477.

40. Greenler, R. G.; Burch, K. D., Stepped single-crystal surfaces as models for small catalyst particles. *Surf. Sci.* **1985,** *152*, 338-345.

41. Bazin, P.; Saur, O.; Lavalley, J. C.; Daturi, M.; Blanchard, G., FT-IR study of CO adsorption on Pt/CeO2: characterisation and structural rearrangement of small Pt particles. *Phys. Chem. Chem. Phys.* **2005,** *7*, 187.

42. Nakamoto, K., *Infrared and Raman Spectra of Inorganic and Coordination Compounds Part B: Applications in Coordination, Organometalic, and Bioinorganic Chemistry*. Sixth ed.; John Wiley & Sons, Inc.: Hoboken, New Jersey, 2009.

43. Oomens, J.; Steill, J. D., Free Carboxylate Stretching Modes. *J. Phys. Chem. A* **2008,** *112*, 3281-3283.

44. Busca, G.; Lorenzelli, V., Infrared spectroscopic identification of species arising from reactive adsorption of carbon oxides on metal oxide surfaces. *Mater. Chem.* **1982,** *7*, 89-126.

45. Ramis, G.; Busca, G.; Lorenzelli, V., Low-temperature CO_2 adsorption on metal oxides: spectroscopic characterization of some weakly adsorbed species. *Mater. Chem. Phys.* **1991,** *29*, 425-435.

46. Ito, K.; Bernstein, H. J., The vibrational spectra of the formate, acetate, and oxalate ions. *Can. J. Chem.* **1956,** *34*, 170-178.

47. Schutte, W. A.; Boogert, A. C. A.; Tielens, A. G. G. M.; Whittet, D. C. B., Weak ice absorption features at 7.24 and 7.41 mu m in the spectrum of the obscured young stellar object W 33A. *Astron. Astrophys.* **1999,** *343*, 966-976.

48. Maçôas, E. M. S.; Lundell, J.; Pettersson, M.; Khriachtchev, L.; Fausto, R.; Räsänen, M., Vibrational spectroscopy of cis- and trans-formic acid in solid argon. *J. Mol. Spectrosc.* **2003,** *219*, 70-80.

49. Canepa, P.; Chiatti, F.; Corno, M.; Sakhno, Y.; Martra, G.; Ugliengo, P., Affinity of hydroxyapatite (001) and (010) surfaces to formic and alendronic acids: a quantum-mechanical and infrared study. *Phys. Chem. Chem. Phys.* **2011,** *13*, 1099-111.

50. Lustemberg, P. G.; Bosco, M. V.; Bonivardi, A.; Busnengo, H. F.; Ganduglia-Pirovano, M. V., Insights into the Nature of Formate Species in the Decomposition and Reaction of Methanol over Cerium Oxide Surfaces: A Combined Infrared Sepctroscopy and Density Functional Theory Study. *J. Phys. Chem. C* **2015,** *119*, 21452-21464.

51. Jacobs, G.; Williams, L.; Graham, U.; Sparks, D.; Davis, B. H., Low-Temperature Water-Gas Shift: In-Situ DRIFTS- Reaction Study of a Pt/CeO_2 Catalyst for Fuel Cell Reformer Applications. *J. Phys. Chem. B* **2003,** *107*, 10398-10404.

52. Grabow, L.; Gokhale, A.; Evans, T. S.; Dumesic, J. A.; Mavrikakis, M., Mechanism of the Water Gas Shift Reaction on Pt: First Principles, Experiments, and Microkinetic Modeling. *J. Phys. Chem. C* **2008,** *112*, 4608-4617.

53. Knell, A.; Barnickel, P.; Baiker, A.; Wokaun, A., CO Oxidation over Au/ZrO_2 Catalysts: Activity, Deactivation Behavior, and Reaction Mechanism. *J. Catal.* **1992,** *137*, 306-321.

54. Hilaire, S.; Wang, X.; Luo, T.; Gorte, R. J.; Wagner, J., A comparative study of water-gas-shift reaction over ceria supported metallic catalysts. *Appl. Catal., A* **2001,** *215*, 271-278.

55. Phatak, A. A.; Delgass, W. N.; Ribeiro, F. H.; Schneider, W. F., Density Functional Theory Comparison of Water Dissociation Steps on Cu, Au, Ni, Pd and Pt. *J. Phys. Chem. C* **2009,** *113*, 7269-7276.

56. Palecek, D.; Tek, G.; Lan, J.; Iannuzzi, M.; Hamm, P., Characterization of the Platinum-Hydrogen Bond by Surface-Sensitive Time-Resolved Infrared Spectroscopy. *J. Phys. Chem. Lett.* **2018,** *9*, 1254-1259.

57. Morrow, B. A.; Ramamurthy, P., Infrared Spectra of Hydroxyl Groups on the Surface of Platinum. *Can. J. Chem.* **1971,** *49*, 3409-3410.

58. Jacobs, G.; Davis, B. H., Surface interfaces in low temperature water-gas shift: The metal oxide synergy, the assistance of co-adsorbed water, and alkali doping. *Int. J. Hydrogen Energy* **2010,** *35*, 3522-3536.

59. Shido, T.; Iwasawa, Y., Reactant-Promoted Reaction Mechanism for Water-Gas Shift Reaction on Rh-Doped CeO_2. *J. Catal.* **1993,** *141*, 71-81.

TOC GRAPHIC